In vivo near infrared fluorescence imaging and dynamic quantification of pancreatic metastatic tumors using folic acid conjugated biodegradable mesoporous silica nanoparticles

Hanrui Li, BS[a,1], Ke Li, PhD[b,1], Yunpeng Dai, PhD[a], Xinyi Xu, PhD[a], Xu Cao, PhD[a],
Qi Zeng, PhD[a], Huyulong He, BS[a], Liaojun Pang, PhD[a], Jimin Liang, PhD[a],
Xueli Chen, PhD[a,*], Yonghua Zhan, PhD[a,c,**]

[a]*Engineering Research Center of Molecular and Neuro Imaging of the Ministry of Education, School of Life Science and Technology, Xidian University, Xi'an, Shaanxi, China*
[b]*Shaanxi Key Laboratory of Ischemic Cardiovascular Disease, Institute of Basic and Translational Medicine, Xi'an Medical University, Xi'an, Shaanxi, China*
[c]*Xidian-Ningbo Information Technology Institute, Xidian University, Xi'an, Shaanxi, China*

Abstract

Cancer metastasis is one of the biggest challenges in cancer treatments since it increases the likelihood that a patient will die from the disease. Therefore, the availability of techniques for the early detection and quantification of tumors is very important. We have prepared cyanine 7.5 NHS ester ($Cy_{7.5}$) and folic acid (FA) conjugated biodegradable mesoporous silica nanoparticles (bMSN@$Cy_{7.5}$-FA NPs) (~100 nm) for visualizing tumors *in vivo*. The fluorescence spectra revealed that the emission peak of bMSN@$Cy_{7.5}$-FA NPs had a red-shift of 1 nm. Confocal immunofluorescent images showed that bMSN@$Cy_{7.5}$-FA NPs had an excellent targeting ability for visualizing cancer cells. *In vivo* fluorescence imaging has been conducted using an orthotopic model for pancreatic cancer within 48 h, and the fluorescence intensity reached a maximum at a post injection time-point of 12 h, which demonstrated that the use of bMSN@$Cy_{7.5}$-FA NPs provides an excellent imaging platform for tumor precision therapy in mice.
© 2018 Elsevier Inc. All rights reserved.

Key words: Tumor metastasis; Mesoporous silica nanoparticles; Fluorescence imaging; Folic acid; Quantification; Pancreatic cancer

Cancer is a major concern to healthcare systems around the world, where it is currently the second leading cause of death in the world.[1] Research by Siegel *et al* has estimated that >600,000 patients will die of cancer in 2017 in the United States, equivalent to around 1650 deaths per day,[2] with pancreatic cancer currently the fourth most common cause of cancer-related deaths.[3,4] Metastasis is a key step in the cancer progression process that represents a significant challenge to developing effective cancer treatment, where it causes pain and many other symptoms that ultimately lead to 90% of deaths for certain types of cancer.[5] Unfortunately, the clinical symptoms of many cancers are often only expressed in the later stages of the disease, which often results in poor patient prognosis. Therefore, early detection and quantification of tumor metastasis is crucial for

cancer diagnosis, since early detection can result in treatments that can improve the survival rate of patients significantly.[6]

Molecular imaging technology plays an important role in the early detection and treatment of cancers by providing a visualization platform for prompt clinical diagnosis.[7] Various imaging technologies are available, such as computed tomography (CT), magnetic resonance imaging (MRI), optical imaging, positron emission tomography (PET), single-photon emission computed tomography (SPECT) and photoacoustic imaging (PA). Amongst these approaches, fluorescence imaging (FI) is considered to be one of the best techniques for early tumor diagnosis and quantification, because it is cost effective, highly sensitive and radiation free[4,7–9]. For example, Zhang *et al* have developed a molecular imaging agent for detecting breast cancer metastasis using positron emission tomography and near-infrared FI.[10] Qiao *et al* employed NaGdF4:Yb,Er core nanoparticles to carry out lymph node metastasis imaging studies using FI,[11] whilst Takashi *et al* used an orthotopic gastric carcinoma model for tumor detection by FI.[12] Christensen *et al* have employed green fluorescence protein labeled tumor cells to monitor tumor growth over a 40 day period using FI, without the need for an external fluorescent probe.[13] Furthermore, Dai *et al* were able to quantify the size of subcutaneous tumors using dynamic FI using a $Cy_{5.5}$-labeled cyclic 9-mer peptide probe.[14]

Mesoporous silica nanoparticles (MSN NPs) are considered to be one of the most useful nanocarriers for imaging applications, because they are formed with large surface areas and high loading capacities, they are easily prepared using synthetic protocols that can be adapted to control particle and pore size, and they contain reactive functional groups that can be modified to attach cell-directing ligands to their surfaces.[15–17] For example, Chan *et al* prepared modified multifunctional MSN NPs for *in vitro* and *in vivo* dual-mode tumor targeted imaging studies,[18] whilst Zeiderman *et al* synthesized MSN NP coated gold nanorods for use as theranostic particles for tumor imaging studies.[19] Furthermore, a range of biodegradable MSN NPs (bMSN NPs) have been developed that exhibit low toxicity levels *in vivo*. In this respect, Shreya *et al* conducted tumor targeting imaging studies using radiolabeled bMSN NPs,[20] whilst Yang *et al* employed glutathione-responsive bMSN NPs to selectively deliver proteins to cancer cells.[21]

The major obstacles in the diagnosis and treatment of cancer is targeted drug delivery in specific tumor sites in the body. One of the strategies to solve this problem is to modify the surface of NPs with target ligands. As a common target ligands, folic acid (FA) enables selectively binding to folate receptors (FRs) that overexpressed in the cell surface in many human tumors including breast, ovary, endometrium, kidney, lung, head and neck, brain, and myeloid cancers.[22,23] As a promising targeting agent, FA has received great attention because its high stability, low cost, non-immunogenicity, ability to be conjugated with a variety of NPs.[24,25] Therefore, the FA ligand is considered as a useful molecule to develop an efficient tumor specific delivery for NPs.

In this study, we now report the design and synthesize of novel cyanine 7.5 NHS ester ($Cy_{7.5}$) and folic acid (FA) conjugated bMSN NPs (bMSN@$Cy_{7.5}$-FA NPs, 100 nm) as imaging agents for the detection and quantification of tumor metastasis. *In vitro* cytotoxicity test results have shown that these monodisperse bMSN NPs are non-toxic, have good biocompatibility, and exhibit good targeted cellular uptake levels, where they accumulate in the cytoplasm of tumor cells. Finally, we have shown that these new bMSN@$Cy_{7.5}$-FA NPs can be used for imaging and quantifying tumors *in vivo* in an established orthotopic model for pancreatic cancer in mice.

Methods

Materials

Hexadecyltrimethylammonium chloride (CTAC, 97%) was purchased from Aladdin. Tetraethyl orthosilicate (TEOS, 99%), triethylamine (TEA, 99.5%), (3-aminopropyl)-triethoxysilane (APS, 99%) and *N*-(3-dimethylaminopropyl)-*N*'-ethylcarbodiimide hydrochloride (EDC) were purchased from Sigma-Aldrich. Folic acid (97%) was purchased from Sigma and *N*-Hydroxysuccinimide (NHS, 98%) was purchased from Aldrich. $Cy_{7.5}$ was obtained from Lumiprobe Life science solutions. All reagents and solvents were used as received, without further purification.

Synthesis of bMSN NPs

bMSN NPs were synthesized as described previously,[26] using an improved method for oil-water biphasic stratification. Therefore, 24 mL of CTAC (25 wt%), 180 mg of TEA and 34 mL of deionized (DI) water were stirred at 60 °C for 1 h. 20 mL of TEOS-cyclohexane solution (1 mL of TEOS and 19 mL of cyclohexane) was then added and the biphasic mixture stirred for 20 h. The desired NPs collected by centrifugation and then washed with NaCl-methanol solution (1 v/v%) to remove the CTAC template, before being dissolved in absolute ethanol.

Synthesis of bMSN@$Cy_{7.5}$-FA NPs

10 mL of the bMSN NPs solution and 10 mL of absolute ethanol were mixed with 1 mL of APS, to give a reaction mixture that was stirred at 88 °C for 48 h. The resultant bMSN-NH$_2$ NPs were obtained by centrifugation and washed with absolute ethanol, before the bMSN-NH$_2$ NPs were dissolved in DI water. 100 μL of the bMSN-NH$_2$ NPs solution was then added to 5 μL of a solution of $Cy_{7.5}$ (5mg mL^{-1}, in DMSO) and the resultant mixture stirred for 2 h in the dark to afford bMSN@$Cy_{7.5}$ NPs.

FA conjugated bMSN@$Cy_{7.5}$ NPs (bMSN@$Cy_{7.5}$-FA NPs) were prepared using the following protocol: 10.8×10^{-6} mol of FA were dispersed in 500 μL of DMSO, followed by addition of 10.8×10^{-6} mol of EDC and 5.4×10^{-5} mol of NHS. The reaction mixture was stirred for 0.5 h, then the bMSN@$Cy_{7.5}$ NPs was added and the reaction mixture stirred for further 3 h in the dark. Unreacted reagents were then separated by centrifugation.

Characterization of NPs

The size and morphology of the bMSN NPs were characterized using a JEOL JEM-2100 transmission electron microscope (TEM). The biodegradation experiments *in vitro* were carried out by immersing and stirring bMSN NPs' sample in the Lactated Ringer's solution at 37 °C with slight shaking.[17]

Their surface zeta potentials and hydrodynamic sizes were measured using a Malvern Zetasizer Nano ZS, whilst their UV absorption spectra were measured using a UV-Visible Spectrophotometer. Fluorescence spectra were obtained using fluorescence spectrometer (F-7000), with fluorescent intensities recorded using IVIS imaging system. The *in vitro* photostability experiments of bMSN@$Cy_{7.5}$-FA NPs were carried out in DI with room light for 12 h and 24 h.

Cell lines and animals model

A549, HEPG2 and BxPC-3 cell lines were provided by Xi'an Medical University. All cell lines were maintained in complete DMEM solution, supplemented with 10% (w/w) FBS and penicillin-streptomycin (76 and 36 U mL^{-1}, respectively). Cells were incubated under 5% CO_2 at 37 °C in a cell incubator (MCO-18AIC, Sanyo, Japan) before being used for *in vitro* tests or for mice inoculation. Nude male mice (4 weeks old, approximately 18 g) were purchased from the Department of Experimental Animals, Health Science Center, Xi'an Jiaotong University. Mice were fed in a SPF animal room whose temperature was maintained at 20 °C. BxPC-3 luciferase tumor-bearing nude mice were obtained by inoculating their pancreases with 5×10^5 of the required cells in 20 μL of PBS. All animal studies were conducted under a protocol approved by the University of Xi'an Jiaotong Animal Care and Use Committee (Number XJTULAC 2016-412).

Stability of bMSN NPs

The stability of the bMSN NPs was determined by measuring the size distribution of samples in PBS and 10% FBS at different temperatures over a period of 12 days, with all data presented as mean values with ± SD (n = 3).

Cellular uptake and affinity assay

The cellular uptake of the NPs was determined using a fluorescent microscope (Eclipse Ti-S, Nikon, Japan). Cells were cultured for 48 h in 3.5 cm confocal dishes, with bMSN@$Cy_{7.5}$-FA NPs being coated to the glass of each well. A confocal microscope (TCS SP5 II, Leica, Germany) with a laser excitation at 458 and 514 nm was used for detection. Endocytosis of the bMSN@$Cy_{7.5}$-FA NPs was determined by monitoring their cellular uptake behavior using a fluorescent microscope and a confocal laser scanning microscope (CLSM). A549, HEPG2 and BxPC-3 cells attached to 6-well plates were incubated with bMSN@$Cy_{7.5}$-FA NPs in the dark for a predetermined time, after which time the cells were rinsed twice with PBS, and visualized using an inverted fluorescence microscope (Eclipse Ti–S, Nikon, Japan). For confocal microscopy, cells in 6-well plates fitted with a cover glass were treated with NPs using the same protocol described above. After incubation in the dark for a predetermined time, the cells were then rinsed with PBS and fixed with 4% paraformaldehyde solution. The effect of FA blocking on cells was determined using cellular affinity analysis using A549, HEPG2 and BxPC-3 cells. All cell lines were cultured for 48 h in 24-well flat-bottomed plates, with control cells incubated with bMSN@$Cy_{7.5}$-FA NPs for 24 h, respectively. Blocked cells were incubated with FA for 24 h prior to addition of bMSN@$Cy_{7.5}$-FA NPs. The fluorescent intensity of cell lines was determined by staining their nuclei using 4',6-diamidino-2-phenylindole (DAPI).

Cytotoxicity assay

The MTT method was employed to test the viability of A549, BxPC-3 and HEPG2 cells in the presence of bMSN@$Cy_{7.5}$-FA NPs, with cells without NPs being used as a control. Cells were seeded onto 96-well flat-bottomed plates with a density of 1×10^5 cells per well and incubated under a 5% CO_2 atmosphere at 37 °C. After 24 h of incubation, the cells were washed with PBS and complete medium containing different concentrations of bMSN@$Cy_{7.5}$-FA NPs added to each well. After 72 h, the medium was replaced with a fresh batch of medium, with 20 μL of MTT solution (5 mg mL^{-1}) then added to each well. The cells were then incubated for an additional 4 h under the same conditions and then the medium containing MTT removed and 100 μL of DMSO added to each well. Absorbances were measured at 590 nm using an ELISA plate reader (Infinite® 200 Pro, Tecan, Switzerland). The *in vitro* cytotoxicity of bMSN@$Cy_{7.5}$-FA NPs was measured using the MTT assay described above. In addition, *in vitro* cytotoxicity of FA was measured using the same method.

In vivo imaging of lymph nodes

Fluorescence intensity and metabolic studies were carried out *in vivo*, with bMSN@$Cy_{7.5}$-FA NPs (100 μL) injected into the left hind paw of each mouse. Mice were then anesthetized using isoflurane and maintained in an anesthetized state throughout the imaging procedures. Mice were imaged with IVIS imaging system using 740 nm excitation light source and 790 nm band-pass emission filter (exposure time is 1 s) with images collected after 0 h, 6 h, 12 h and 24 h, respectively.

In vivo FI and image analysis

An orthotopic metastasis pancreatic tumor model in nude mice was used to accurately visualize the position and volume of tumors. 100 μL of firefly luciferase (30 mg mL^{-1}) was injected into mice, with luminous images then being collected using the IVIS imaging system after 10 minutes. The *in vivo* fluorescence images were then visualized at 0.5 h, 3 h, 12 h and 48 h after injection with bMSN@$Cy_{7.5}$-FA NPs, using a 740 nm excitation light source and a 790 nm band-pass emission filter (exposure time of 1 s). The mice were divided into three groups: targeted, non-targeted and blocking. The mice within the targeted and non-targeted groups were then injected with 200 μL of bMSN@$Cy_{7.5}$-FA NPs and bMSN@$Cy_{7.5}$ NPs into their tail veins, respectively. The blocking group were injected with FA 3 h before being further injected with 200 μL of bMSN@$Cy_{7.5}$-FA NPs. Dynamic imaging of orthotopic metastasis mice was performed 0.5 h after intravenous injection of the bMSN@$Cy_{7.5}$-FA NPs. Serial fluorescence images were collected every 18 seconds using an exposure time set at 1 s. Furthermore, organs from these mice, including heart, liver, spleen, lungs, kidneys and tumors, were collected and analyzed using the IVIS imaging system.
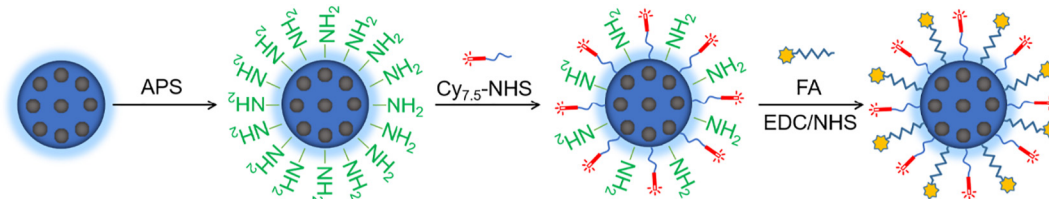
Figure 1. Synthesis of bMSN@Cy$_{7.5}$-FA NPs.

Image processing and analysis were conducted using Matlab 2015b (The Math Works, Inc., Natick, MA) with regions of interest (ROIs) visualized using Living Image 4.5 software. For quantitative analysis, tumor ROIs were determined using white light images, whilst muscle regions of similar size that were positioned contralateral to tumors selected as muscle ROI. The mean value of fluorescent signals within each ROI were calculated after background values were subtracted from each fluorescent image. This enabled fluorescence activity versus time curves (TACs) of tumor and muscle ROIs of the fluorescent images to be determined accurately.[14,27]

Kinetic model and parameter estimation

The model used for analysis of the bMSN@Cy$_{7.5}$-FA NP data assumed that there three possible environments could be occupied, so a two-tissue (three-compartment) model was used to describe bMSN@Cy$_{7.5}$-FA NP kinetics. This model involves consideration of (i) the amount of non-metabolized tracer in the blood plasma compartment (C$_P$); (ii) the amount of free and non-specific binding tracer (non-displaceable uptake) in the extra-vascular and intracellular space (C$_{ND}$); and (iii) the amount of tracer specifically bound to the receptor (C$_S$). The following image shows a three-compartment model that uses a Gurfinkel exponential model (GEXPM) to describe the kinetics of bMSN@Cy$_{7.5}$-FA NPs distribution in tumor tissues. K$_1$ is the tracer extravasation rate into tissues; k$_2$ reflects the non-displaceable uptake tissue efflux rate from interstitial space into plasma; k$_r$ reflects the rate of tracer accumulation in the second tissue compartment, whether through binding to the receptor, or internalization; whilst k$_{el}$ is the rate of tracer elimination in plasma via other routes such as kidney filtration and liver metabolism.
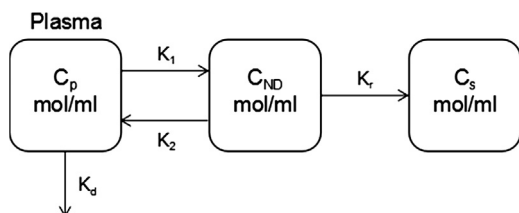
According to this model, GEXPM can be expressed as Eq. (1)[28]

$$I(t) = A[1 - \exp(-\alpha t)] + B[1 - \exp(-\beta t)] \tag{1}$$

where the fluorescence activity of the tracer in the tumor or muscle tissues is given by I(t); A and B are macro-parameters that describe the magnitude of the detected signal; and α and β

are macro-parameters that describe receptor-ligand affinity. In this study, we were mostly concerned with determining the α + β values of the tumor tissue, which represents the sum of the pharmacokinetic rate constants that is equal to k$_1$ + k$_2$ + k$_r$ + k$_{el}$.

Statistical analysis

Data are given as the mean values ± SD of independent repeat experiments, with a P-value <0.05 considered to represent a statistically significant difference between comparative data.

Results

Synthesis and characterization of bMSN@Cy$_{7.5}$-FA NPs

The bMSN@Cy$_{7.5}$-FA NPs were prepared according to the protocol described in Figure 1. As shown in Figure 2, *A*, TEM results showed that the resultant bMSN NPs had uniform particle size, good monodispersity, with clear and ordered mesoporous structures with an average diameter of ~100 nm. DLS measurements further verified that the bMSN NPs had an average hydrodynamic diameter of 102.6 ± 0.2 nm (Figure 2, *B*). The zeta-potential value of the bMSN-NH$_2$ NPs was determined to be 31.3 ± 0.7 mV (Figure S1). After conjugation with Cy$_{7.5}$ and FA, the zeta-potential value of the bMSN@Cy$_{7.5}$ NPs was 24.3 ± 0.4 mV (Figure S2), whilst the zeta-potential of the bMSN@Cy$_{7.5}$-FA NPs was -24.8 ± 0.4 mV (Figure S3). Figure 1, *C* shows the UV absorption spectra of bMSN NPs, Cy$_{7.5}$, FA and bMSN@Cy$_{7.5}$-FA NPs, with the broadening of the absorption spectra of bMSN@Cy$_{7.5}$-FA. Moreover, the degradation experiment also proved that the bMSN NPs was biodegradable (Figure S4). The fluorescence spectra of Cy$_{7.5}$ and bMSN@Cy$_{7.5}$-FA NPs (Figure 2, *D*) revealed that the emission peak of bMSN@Cy$_{7.5}$-FA NPs had a red-shift of 1 nm when compared with free Cy$_{7.5}$. The fluorescence intensities of Cy$_{7.5}$ and bMSN@Cy$_{7.5}$-FA NPs at different concentrations are shown in Figures S5, *A*, *C*, with Figure S5, *B*, *D* showing that their fluorescence intensities correlated almost linearly to their concentration. The photostability experiments *in vitro* showed that the fluorescence intensity had hardly changed after 24 h (Figure S6). The stability of bMSN@Cy$_{7.5}$-FA NPs was measured at different temperatures (see Figure S7), the size of bMSN@Cy$_{7.5}$-FA NPs did not change significantly over 12 days, with the solution remaining clear with no evidence of any precipitation.

Cellular uptake and affinity assay

A549, HEPG2 and BxPC-3 were used as model cell lines to assess their cellular uptake ability *in vitro* (See Figure 3).
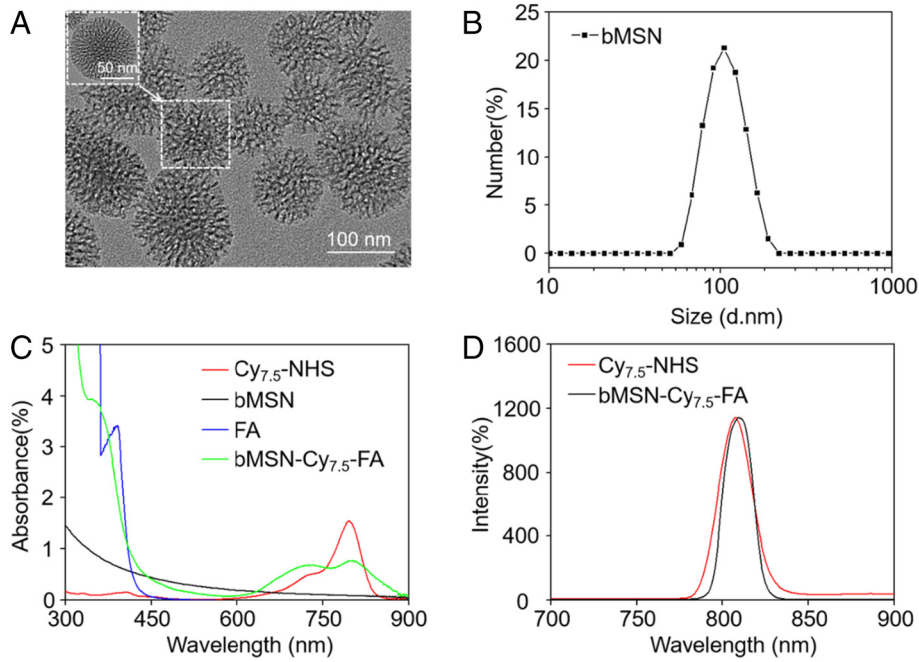
Figure 2. Characterization of bMSN@Cy$_{7.5}$-FA NPs. (**A**) TEM images of bMSN NPs; (**B**) Size distribution of bMSN NPs determined using DLS. (**C**) UV absorption spectra of Cy$_{7.5}$, bMSN NPs, FA and bMSN@Cy$_{7.5}$-FA NPs. (**D**) Fluorescence spectra of C$_{7.5}$ and bMSN@Cy$_{7.5}$-FA NPs.
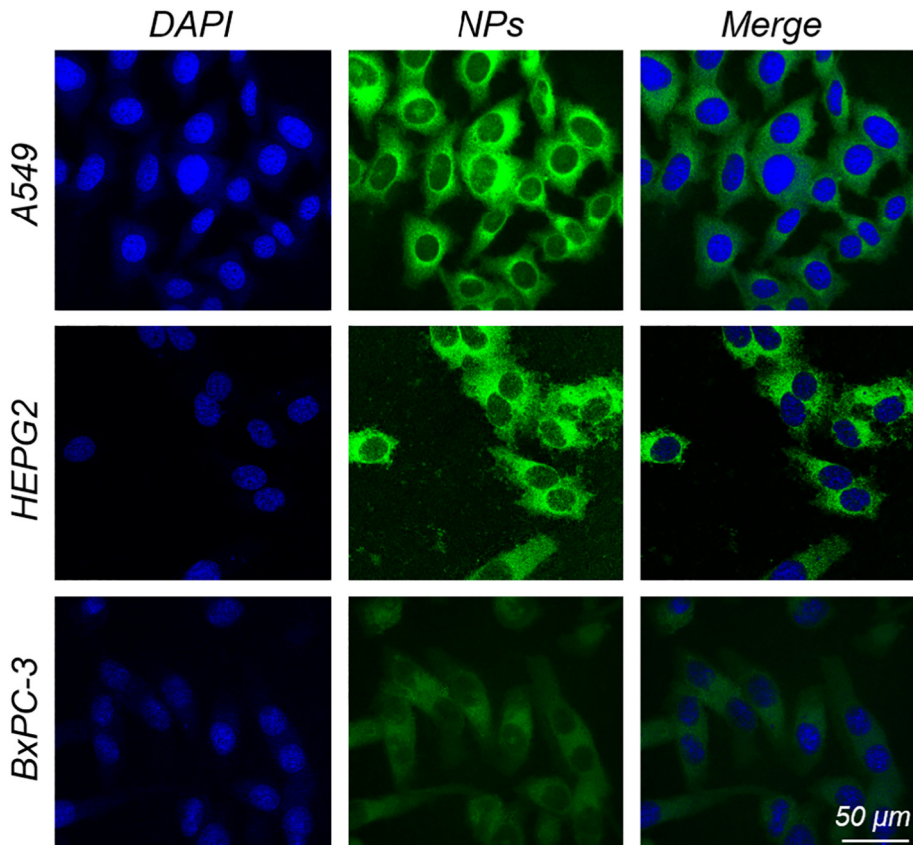

Figure 3. Confocal immunofluorescent images of bMSN@Cy$_{7.5}$-FA NPs showing their expression and localization in A549, HEPG2 and BxPC-3 cells. Cells stained with DAPI are colored blue. Cells containing bMSN@Cy$_{7.5}$-FA NPs are colored green.
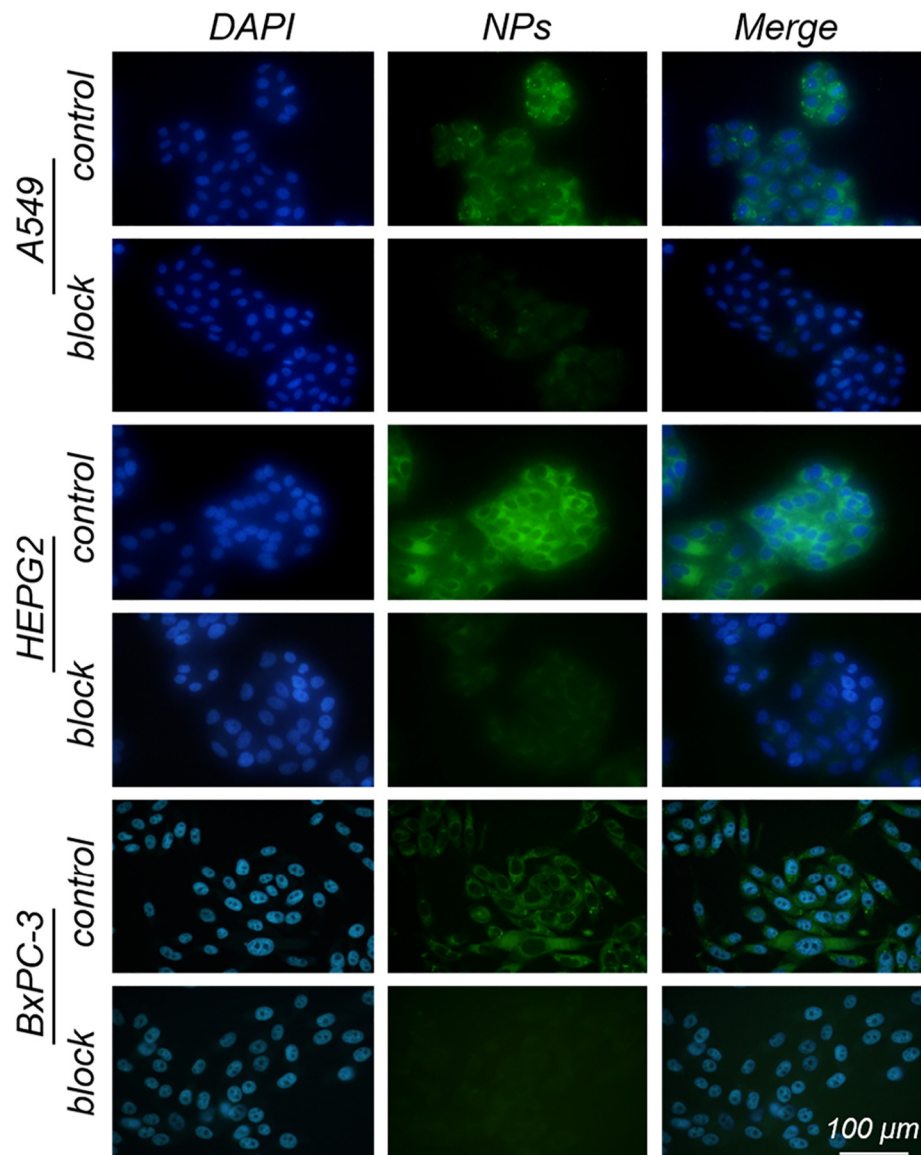
Figure 4. Confocal immunofluorescent images of bMSN@Cy$_{7.5}$-FA NPs showing their expression and localization in the presence of FA as a blocking agent in A549, HEPG2 and BxPC-3 cells. Cells stained with DAPI are colored blue. Cells containing bMSN@Cy$_{7.5}$-FA NPs are colored green.

Confocal laser microscopy results revealed that these cell-lines internalized the bMSN@Cy$_{7.5}$-FA NPs, which were found to be distributed throughout the cytoplasm (green) and gathered around the nucleus (blue). The tumor targeting ability of bMSN@Cy$_{7.5}$-FA NPs were explored using an affinity assay (see Figure 4), which revealed that the fluorescence intensity of cells exposed to bMSN@Cy$_{7.5}$-FA NPs in the presence of a FA blocking group was significantly reduced when compared to a control group. In addition, the quantitative analysis of fluorescence intensity also showed the same results (Figure S8).

Cytotoxicity assay

The cytotoxicity of bMSN@Cy$_{7.5}$-FA NPs was evaluated using an MTT assay. As can be seen from Figure S9, no significant cytotoxicity from the bMSN@Cy$_{7.5}$-FA NPs was observed at concentrations from 0.003 to 0.3 mg mL^{-1}. Similarly, the FA was also non-toxic to cancer cells (Figure S10).

In vivo Lymph Node imaging

Lymph node imaging studies were carried out by injecting bMSN@Cy$_{7.5}$-FA NPs into mice that were then imaged. As shown in Figure 5, *A*, the popliteal lymph nodes had obvious signal enhancement (red circle), with fluorescence intensity found to be at its highest after 12 h. The fluorescent response for the ischial lymph nodes could also be observed clearly (green circle). The black and red lines in Figure 5, *B* show the fluorescence intensity variations between popliteal lymph nodes and ischial lymph nodes, respectively. These fluorescence intensity curves show increasing fluorescence in the first 0-12 h, followed by a decrease in intensity after 12 h.
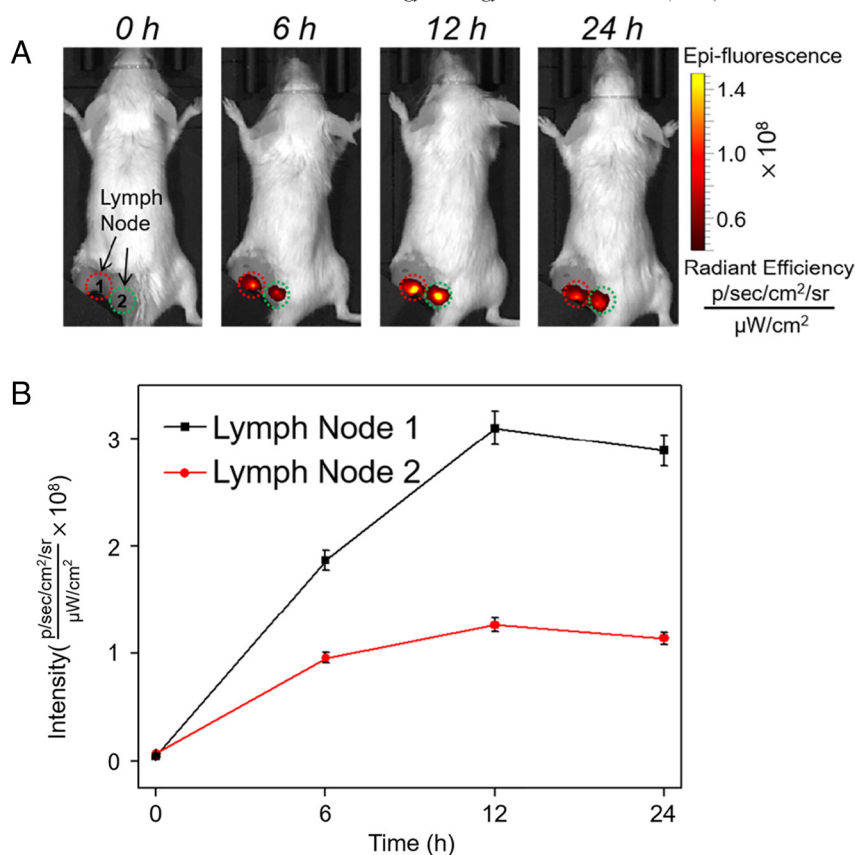
Figure 5. Lymph node imaging after intradermal injection of bMSN@Cy$_{7.5}$-FA NPs. (**A**) Fluorescent images at 0 h, 6 h, 12 h and 24 h post-injection with bMSN@Cy$_{7.5}$-FA NPs. (**B**) Fluorescent intensity of lymph nodes at different times.

In vivo FI and dynamic quantification of the tumor metastasis

Fluorescence images were obtained by IVIS imaging. As shown in Figure 6, tumor metastasis sites were first located using bioluminescence imaging studies. The fluorescence intensity of the targeted group was found to be significantly higher than for the non-targeted group, with signal intensities reaching a maximum after 12 h. Intraperitoneal injection of FA as a blocking group resulted in a small decrease in fluorescence intensity. Two tumors that were located away from the liver were chosen for analysis in each mouse (red circle and black circle), which enabled the fluorescent responses of ROIs to be determined accurately. The curves of fluorescence intensity for these tumors after 48 h are shown in Figure S11, with the black square line describing intensity variations of the targeted group; the red circle line showing the intensity variations of the non-targeted group; and the blue triangle line corresponding to the intensity variations of the blocking group. It is worth noting that significant fluorescence signal enhancement around tumors was present 0.5 h after injection in all three groups. At a post injection time-point of 12 h, the fluorescence intensity of the targeted group reached a maximum that was 1.7 times greater that the fluorescence intensity of the FA blocking group. And the fluorescence intensity of the tumor decreased in all three groups after 12 h. As shown in Figure S12, *A*, all the mice from the three groups were sacrificed and their organs and tumors were removed for fluorescent analysis. As can be seen in Figure

S12, *B*, the fluorescence intensity of the liver was strong, with the intensity of the tumor in the targeted NP group stronger than that for the non-targeted and blocking NP groups. Furthermore, staining of the major organs (heart, liver, spleen, lungs, and kidneys) with hematoxylin and eosin (H&E) for histological analysis, revealed no obvious tissue damage to these organs (Figure S13).

The FI of tumor and muscle within 30 minutes were determined using the IVIS system and bioluminescence images of ROIs acquired. As shown in Figure 7, *A*, an obvious fluorescence intensity enhancement was observed in the region of tumor, with no significant intensity change in the muscle region. Figure 7, *B* shows raw time activity curves and their corresponding nonlinear fitting results in tumor and muscle tissues, which reveal that the rate of tracer uptake in tumor tissue was greater than for muscle tissue.

Discussion

bMSN NPs were synthesized using an improved oil-water biphasic stratification method, employing the cationic surfactant CTAC as a template, TEOS as a silica source, TEA as a catalyst and cyclohexane as an emulsifying agent.[26,29] TEM results showed that the resultant bMSN NPs had an average diameter of ~100 nm. DLS measurements further verified that the bMSN NPs had an average hydrodynamic diameter of 102.6 ± 0.2 nm.
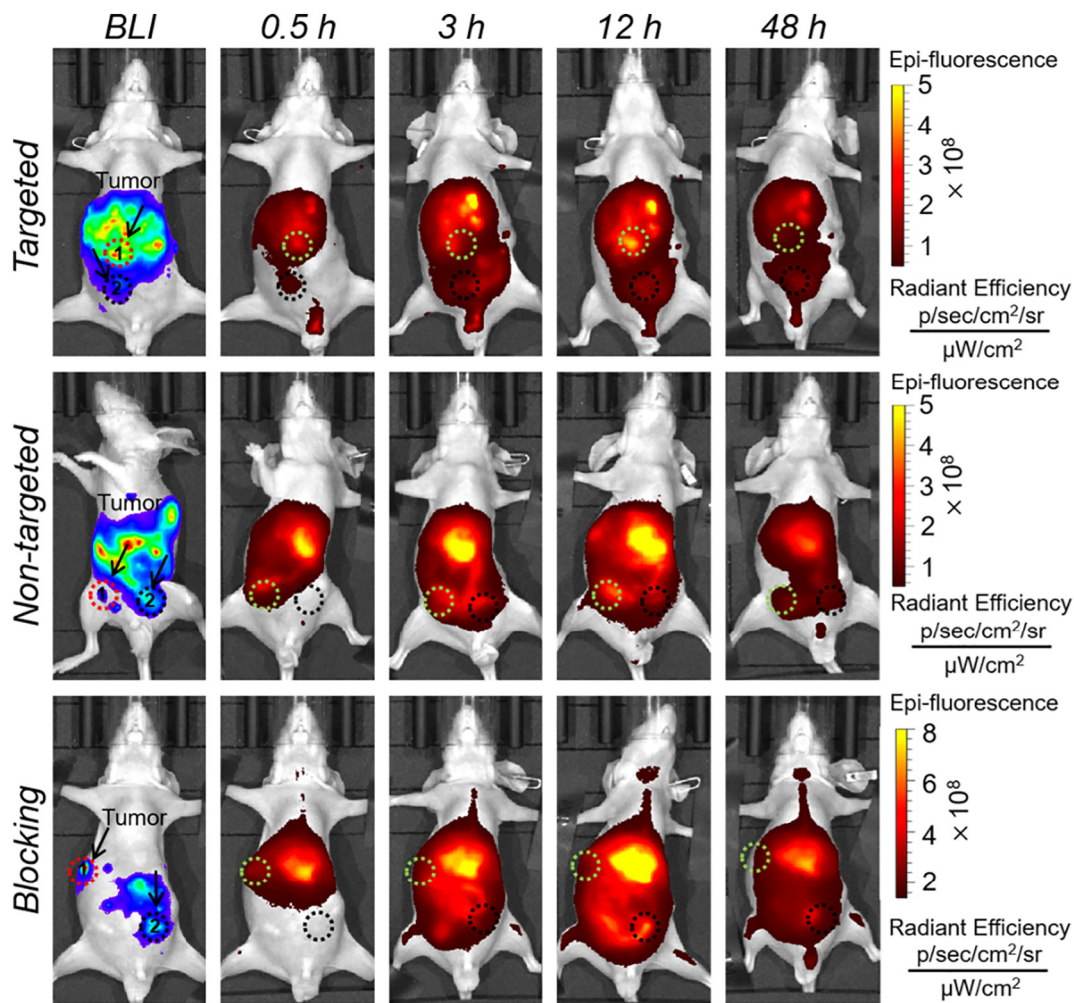
Figure 6. *In vivo* bioluminescent imaging and fluorescence imaging of bMSN@Cy$_{7.5}$-FA NPs in cells after 48 h.

The particle size of the bMSN NPs measured using TEM analysis is slightly smaller than the results obtained using hydrodynamic diameter measurement, because of loss of solvent during TEM analysis.[23] The zeta-potential value of the bMSN-NH$_2$ NPs was determined to be 31.3 ± 0.7 mV, thus verifying the presence of their NH$_2$ groups. After conjugation with Cy$_{7.5}$ and FA, the zeta-potential value of the bMSN@Cy$_{7.5}$ NPs was 24.3 ± 0.4 mV, whilst the zeta-potential of the bMSN@Cy$_{7.5}$-FA NPs was -24.8 ± 0.4 mV, suggesting that the amino groups of the bMSN-NH$_2$ NPs had been conjugated successfully. The degradation experiment proved that the bMSN NPs was biodegradable, which was consistent with previous studies.[17] UV absorption and fluorescence spectra were then obtained to provide further evidence that Cy$_{7.5}$ and FA were attached to the surface of the NPs. The broadening of the absorption spectra of bMSN@Cy$_{7.5}$-FA due to encapsulation of Cy$_{7.5}$ by the bMSN NPs. The fluorescence spectra of bMSN@Cy$_{7.5}$-FA NPs revealed that the emission peak of bMSN@Cy$_{7.5}$-FA NPs had a red-shift when compared with free Cy$_{7.5}$. This red-shift may be attributed to inter chain interactions occurring when Cy$_{7.5}$ is coated onto the surface of the bMSN-NH$_2$ NPs. These

interactions may allow more efficient energy transfer from high to low energy states, which could lead to the observed red-shift of the bMSN@Cy$_{7.5}$-FA NPs.[30] The fluorescence intensities of Cy$_{7.5}$ and bMSN@Cy$_{7.5}$-FA NPs at different concentrations showed that their fluorescence intensities correlated almost linearly to their concentration. Furthermore, the photostability experiments also revealed that the light had no effect on the fluorescence intensity of bMSN@Cy$_{7.5}$-FA NPs. The stability of NPs is one of the most important factors for carrying out long-term imaging studies *in vivo*. The results indicated that the bMSN@Cy$_{7.5}$-FA NPs had good stability and excellent potential as agents for carrying out tumor imaging studies.

To further explore the stability and distribution of bMSN@Cy$_{7.5}$-FA NPs *in vivo*, A549, HEPG2 and BxPC-3 were used as model cell lines to assess their cellular uptake ability *in vitro*. Confocal laser microscopy results indicating that bMSN@Cy$_{7.5}$-FA NPs were stable *in vivo* and could potentially be used for *in vivo* imaging applications. Because FA is non-toxic, the fluorescence intensity decreased in block group only caused by FA blocking. Elevated expression of FR has been observed on the surfaces of various cancer cells, which enables it to be used as
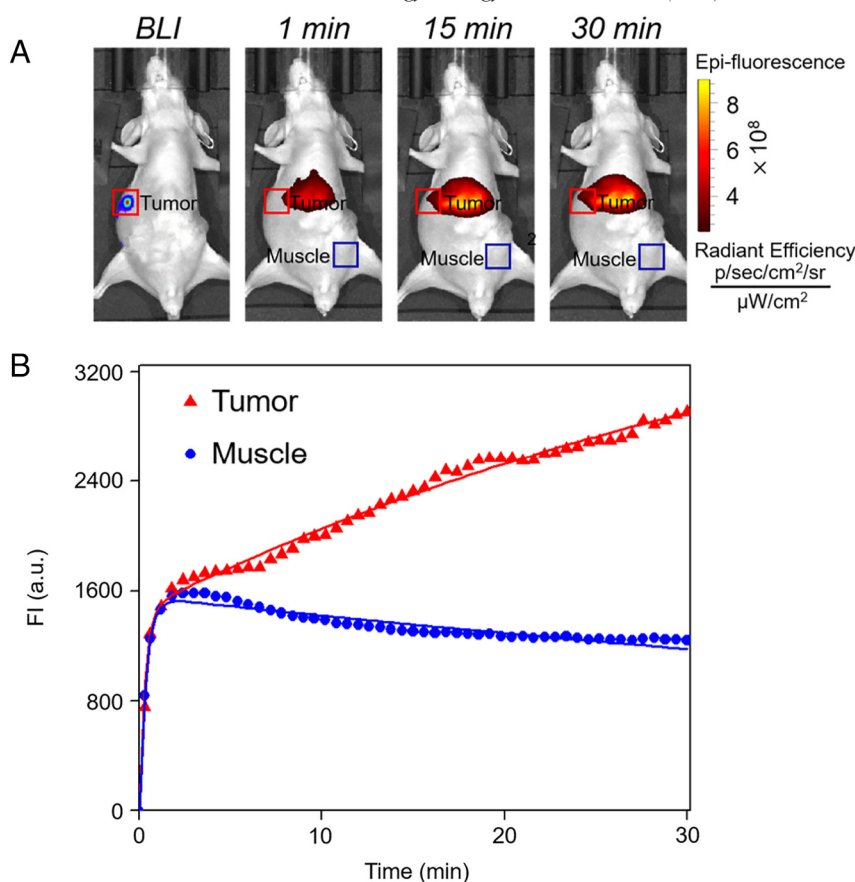
Figure 7. (**A**) Original BLI and fluorescent images (no background subtraction) at different time points, with red and blue squares representing tumor tissue and muscle tissue, respectively. (**B**) Corresponding raw time activity curves for tumor tissue and the muscle tissue. Symbols as previously defined, with solid lines representing the corresponding nonlinear fitting results.

an effective targeting ligand for tumor imaging studies.[31,32] The tumor targeting ability of bMSN@Cy$_{7.5}$-FA NPs were explored using an affinity assay, which revealed that the fluorescence intensity of cells exposed to bMSN@Cy$_{7.5}$-FA NPs in the presence of a FA blocking group was significantly reduced when compared to a control group. This is because FAs can bind strongly to the large number of FRs present on the surface of the cancer cells, which can prevent the bMSN@Cy$_{7.5}$-FA NPs from binding, resulting in a weaker fluorescence response in the presence of FA. Therefore, it can be concluded that the bMSN@Cy$_{7.5}$-FA NPs exhibit favorable targeting ability towards cancer cells that overexpress FR, which could potentially be used for *in vivo* targeted tumor imaging applications.

The cytotoxicity of bMSN@Cy$_{7.5}$-FA NPs was evaluated using an MTT assay. There was no significant cytotoxicity from the bMSN@Cy$_{7.5}$-FA NPs was observed. This result indicates that the bMSN@Cy$_{7.5}$-FA NPs should have little cytotoxicity within the concentration range required for imaging applications.

The lymphatic system plays an important role in the bodies resistance to disease, however it is also a common site of tumor metastasis,[33,34] with accurate detection of the extent of lymph node metastasis essential for the early detection and treatment of cancers. Lymph node imaging was carried out using an IVIS imaging system. The popliteal lymph nodes and the ischial

lymph nodes had obvious signal enhancement. Quantitative changes in the fluorescence intensity of lymph nodes were determined by comparing the fluorescence intensities of each ROI. The fluorescence intensity curves between popliteal lymph nodes and ischial lymph nodes revealed that bMSN@Cy$_{7.5}$-FA NPs readily accumulate in lymph nodes, further demonstrating the potential of these NPs for *in vivo* tumor imaging.

Cancer metastasis is one of the biggest challenges in cancer treatment. Therefore, early detection of cancer is critical to cancer diagnosis.[35] According to the lymph node imaging, we have proved that bMSN@Cy$_{7.5}$-FA NPs can be used for lymph node mapping. It was then decided to determine whether bMSN@Cy$_{7.5}$-FA NPs could be used for targeted imaging of tumors *in vivo*, with an orthotopic metastatic pancreatic tumor model being chosen for screening. The fluorescence intensity of the targeted group was found to be significantly higher than the non-targeted group. Intraperitoneal injection of FA as a blocking group resulted in a decrease in fluorescence intensity, indicating that the bMSN@Cy$_{7.5}$-FA NPs have excellent cellular targeting ability for these cancer cells. Since the hydrodynamic diameter of the bMSN@Cy$_{7.5}$-FA NPs is above the cutoff for renal filtration, it was found that these NPs were primarily cleared through the hepatobiliary pathway.[16,36,37] This accumulation showed that the fluorescence intensity of the liver in whole body images was

found to be greater than the fluorescence intensity of any tumors that were present. Therefore, two tumors that were located away from the liver were chosen for analysis in each mouse, which enabled the fluorescent responses of ROIs to be determined accurately. It is worth noting that significant fluorescence signal enhancement around tumors was present in all three groups. At a post injection time-point of 12 h, the fluorescence intensity of the targeted group reached a maximum that was greater than the fluorescence intensity of the FA blocking group. This is likely to be due to the FA occupying a significant number of FR sites on the surfaces of the tumor cells, thus preventing the bMSN@$Cy_{7.5}$-FA NPs from binding. In order to further verify these *in vivo* imaging results, all the mice were sacrificed and their organs and tumors removed for fluorescent analysis. The fluorescence intensity of the liver was strong, with the intensity of the tumor in the targeted group stronger than that of the non-targeted and blocking groups. Furthermore, staining of the major organs with H&E for histological analysis, revealed no obvious tissue damage to these organs. Therefore, from the above results, it can be concluded that bMSN@$Cy_{7.5}$-FA NPs have excellent tumor targeting ability and they can be used for *in vivo* imaging of tumor metastasis.

Dynamic FI studies were then conducted to accurately correlate bMSN@$Cy_{7.5}$-FA NPs binding to the extent of tumor metastasis.[38] The FI of tumor and muscle within 30 minutes were determined, which further verified the selective binding of bMSN@$Cy_{7.5}$-FA NPs to tumor sites. Furthermore, the increased rate of probe uptake in tumor tissues was reflected in the fitted pharmacokinetic parameters, where $\alpha + \beta$ values represent the sum of both pharmacokinetic rate constants. Therefore, the $\alpha + \beta$ value for tumor tissues of 0.055 was found to be significantly higher than for muscle tissue which gave an $\alpha + \beta$ value of 0.045. All these results indicate that bMSN@$Cy_{7.5}$-FA NPs have good binding ability for FRs that are overexpressed on the surface of certain cancer cells, which should enable them to be employed as FI agents for early detection of tumor metastasis.

Appendix A. Supplementary data

Supplementary data to this article can be found online at https://doi.org/10.1016/j.nano.2018.04.018.

References

1. Torre LA, Siegel RL, Ward EM, Jemal A. Global Cancer Incidence and Mortality Rates and Trends-An Update. *Cancer Epidemiol Biomark Prev* 2016;**25**:16-27.
2. Siegel RL, Miller KD, Jemal A. Cancer Statistics, 2017. *CA Cancer J Clin* 2017;**67**:7-30.
3. Kaushal S, McElroy MK, Luiken GA, Talamini MA, Moossa AR, Hoffman RM, et al. Fluorophore-conjugated anti-CEA Antibody for the Intraoperative Imaging of Pancreatic and Colorectal Cancer. *J Gastrointest Surg* 2008;**12**:1938-50.
4. England CG, Hernandez R, Eddine SBZ, Cai WB. Molecular Imaging of Pancreatic Cancer with Antibodies. *Mol Pharm* 2016;**13**:8-24.
5. Schroeder A, Heller DA, Winslow MM, Dahlman JE, Pratt GW, Langer R, et al. Treating metastatic cancer with nanotechnology. *Nat Rev Cancer* 2012;**12**:39-50.
6. Bakhtiary Z, Saei AA, Hajipour MJ, Raoufi M, Vermesh O, Mahmoudi M. Targeted superparamagnetic iron oxide nanoparticles for early detection of cancer: Possibilities and challenges. *Nanomedicine* 2016;**12**:287-307.
7. Weissleder R, Pittet MJ. Imaging in the era of molecular oncology. *Nature* 2008;**452**:580-9.
8. Padmanabhan P, Kumar A, Kumar S, Chaudhary RK, Gulyas B. Nanoparticles in practice for molecular-imaging applications: An overview. *Acta Biomater* 2016;**41**:1-16.
9. Hilderbrand SA, Weissleder R. Near-infrared fluorescence: application to in vivo molecular imaging. *Curr Opin Chem Biol* 2010;**14**:71-9.
10. Zhang Y, Hong H, Nayak TR, Valdovinos HF, Myklejord DV, Theuer CP, et al. Imaging tumor angiogenesis in breast cancer experimental lung metastasis with positron emission tomography, near-infrared fluorescence, and bioluminescence. *Angiogenesis* 2013;**16**:663-74.
11. Qiao R, Liu C, Liu M, Hu H, Liu C, Hou Y, et al. Ultrasensitive in Vivo Detection of Primary Gastric Tumor and Lymphatic Metastasis Using Upconversion Nanoparticles. *ACS Nano* 2015;**9**:2120-9.
12. Murakami T, Zhang Y, Wang X, Hiroshima Y, Kasashima H, Yashiro M, et al. Orthotopic Implantation of Intact Tumor Tissue Leads to Metastasis of OCUM-2MD3 Human Gastric Cancer in Nude Mice Visualized in Real Time by Intravital Fluorescence Imaging. *Anticancer Res* 2016;**36**:2125-30.
13. Christensen J, Vonwil D, Shastri VP. Non-Invasive In Vivo Imaging and Quantification of Tumor Growth and Metastasis in Rats Using Cells Expressing Far-Red Fluorescence Protein. *PLoS One* 2015;**10**, https://doi.org/10.1371/journal.pone.0132725.
14. Dai Y, Yin J, Huang Y, Chen X, Wang G, Liu Y, et al. In vivo quantifying molecular specificity of Cy5.5-labeled cyclic 9-mer peptide probe with dynamic fluorescence imaging. *Biomed Opt Express* 2016;**7**:1149-59.
15. He Q, Shi J. MSN Anti-Cancer Nanomedicines: Chemotherapy Enhancement, Overcoming of Drug Resistance, and Metastasis Inhibition. *Adv Mater* 2014;**26**:391-411.
16. Tang FQ, Li LL, Chen D. Mesoporous Silica Nanoparticles: Synthesis, Biocompatibility and Drug Delivery. *Adv Mater* 2012;**24**:1504-34.
17. Shen DK, Yang JP, Li XM, Zhou L, Zhang RY, Li W, et al. Biphase Stratification Approach to Three-Dimensional Dendritic Biodegradable Mesoporous Silica Nanospheres. *Nano Lett* 2014;**14**:923-32.
18. Chan M-H, Lin H-M. Preparation and identification of multifunctional mesoporous silica nanoparticles for in vitro and in vivo dual-mode imaging, theranostics, and targeted tracking. *Biomaterials* 2015;**46**:149-58.
19. Zeiderman MR, Morgan DE, Christein JD, Grizzle WE, McMasters KM, McNally LR. Acidic pH-Targeted Chitosan-Capped Mesoporous Silica Coated Gold Nanorods Facilitate Detection of Pancreatic Tumors via Multispectral Optoacoustic Tomography. *ACS Biomater Sci Eng* 2016;**2**:1108-20.
20. Goel S, Chen F, Luan SJ, Valdovinos HF, Shi SX, Graves SA, et al. Engineering Intrinsically Zirconium-89 Radiolabeled Self-Destructing Mesoporous Silica Nanostructures for In Vivo Biodistribution and Tumor Targeting Studies. *Adv Sci* 2016;**3**:11, https://doi.org/10.1002/advs.201600122.
21. Yang Y, Wan J, Niu Y, Gu Z, Zhang J, Yu M, et al. Structure-Dependent and Glutathione-Responsive Biodegradable Dendritic Mesoporous Organosilica Nanoparticles for Safe Protein Delivery. *Chem Mater* 2016;**28**:9008-16.
22. Hu H, Dai AT, Sun J, Li XY, Gao FH, Wu LZ, et al. Aptamer-conjugated Mn3O4@SiO2 core-shell nanoprobes for targeted magnetic resonance imaging. *Nanoscale* 2013;**5**:10447-54.
23. Wang K, Huang Q, Qiu F, Sui M. Non-viral Delivery Systems for the Application in p53 Cancer Gene Therapy. *Curr Med Chem* 2015;**22**:4118-36.

24. Yang H, Zhuang YM, Hu H, Du XX, Zhang CX, Shi XY, et al. Silica-Coated Manganese Oxide Nanoparticles as a Platform for Targeted Magnetic Resonance and Fluorescence Imaging of Cancer Cells. *Adv Funct Mater* 2010;**20**:1733-41.

25. Zhang B, Wang K, Si J, Sui M, Shen Y. *Charge-Reversal Polymers for Biodelivery*. Wiley-VCH Verlag GmbH & Co KGaA; 2014223-42.

26. Liut Y, Li W, Shen D, Wang C, Li X, Pal M, et al. Synthesis of Mesoporous Silica/Reduced Graphene Oxide Sandwich-Like Sheets with Enlarged and "Funneling" Mesochannels. *Chem Mater* 2015;**27**:5577-86.

27. Dai Y, Chen X, Yin J, Kang X, Wang G, Zhang X, et al. Investigation of injection dose and camera integration time on quantifying pharmacokinetics of a Cy5.5-GX1 probe with dynamic fluorescence imaging in vivo. *J Biomed Opt* 2016;**21**, https://doi.org/10.1117/1.jbo.21.8.086001.

28. Gurfinkel M, Ke S, Wang W, Li C, Sevick-Muraca EM. Quantifying molecular specificity of alphavbeta3 integrin-targeted optical contrast agents with dynamic optical imaging. *J Biomed Opt* 2005;**10**034019.

29. Wu SH, Mou CY, Lin HP. Synthesis of mesoporous silica nanoparticles. *Chem Soc Rev* 2013;**42**:3862-75.

30. Zhan Y, Zhan W, Li H, Xu X, Cao X, Zhu S, et al. In Vivo Dual-Modality Fluorescence and Magnetic Resonance Imaging-Guided Lymph Node Mapping with Good Biocompatibility Manganese Oxide Nanoparticles. *Molecules* 2017;**22**, https://doi.org/10.3390/molecules22122208.

31. Sudimack J, Lee RJ. Targeted drug delivery via the folate receptor. *Adv Drug Deliv Rev* 2000;**41**:147-62.

32. Yang XY, Zhou ZG, Wang L, Tang CZ, Yang H, Yang SP. Folate conjugated Mn3O4@SiO2 nanoparticles for targeted magnetic resonance imaging in vivo. *Mater Res Bull* 2014;**57**:97-102.

33. Achen MG, Mann GB, Stacker SA. Targeting lymphangiogenesis to prevent tumour metastasis. *Br J Cancer* 2006;**94**:1355-60.

34. Achen MG, McColl BK, Stacker SA. Focus on lymphangiogenesis in tumor metastasis. *Cancer Cell* 2005;**7**:121-7.

35. Collisson EA, Maitra A. Pancreatic Cancer Genomics 2.0: Profiling Metastases. *Cancer Cell* 2017;**31**:309-10.

36. Albanese A, Tang PS, Chan WCW. The Effect of Nanoparticle Size, Shape, and Surface Chemistry on Biological Systems. *Annu Rev Biomed Eng* 2012;**14**:1-16.

37. Zhan Y, Shi S, Ehlerding EB, Graves SA, Goel S, Engle JW, et al. Radiolabeled, Antibody-Conjugated Manganese Oxide Nanoparticles for Tumor Vasculature Targeted Positron Emission Tomography and Magnetic Resonance Imaging. *ACS Appl Mater Interfaces* 2017;**9**:38304-12.

38. Hong GS, Lee JC, Jha A, Diao S, Nakayama KH, Hou LQ, et al. Near-Infrared II Fluorescence for Imaging Hindlimb Vessel Regeneration With Dynamic Tissue Perfusion Measurement. *Circ Cardiovasc Imaging* 2014;**7**:517-25.